Seasonal Variability in Warm-Water Inflow toward Kangerdlugssuaq Fjord

RENSKE GELDERLOOS AND THOMAS W. N. HAINE

Department of Earth and Planetary Sciences, The Johns Hopkins University, Baltimore, Maryland

INGA M. KOSZALKA

GEOMAR Helmholtz Centre for Ocean Research, Kiel, Germany

MARCELLO G. MAGALDI

Istituto di Scienze Marine, Sede Secondaria di Lerici, Consiglio Nazionale delle Ricerche, Lerici, Italy, and Department of Earth and Planetary Sciences, The Johns Hopkins University, Baltimore, Maryland

(Manuscript received 31 August 2016, in final form 14 April 2017)

ABSTRACT

Seasonal variability in pathways of warm-water masses toward the Kangerdlugssuaq Fjord (KF)–Glacier (KG) system, southeast Greenland, is investigated by backtracking Lagrangian particles seeded at the fjord mouth in a high-resolution regional ocean model simulation in the ice-free and the ice-covered seasons. The waters at KF are a mixture of Atlantic-origin water advected from the Irminger Basin [Faxaflói (FF)], the deep waters from the Denmark Strait, and the waters from the Arctic Ocean, both represented by the Kögur section (KO). Below 200-m depth, the warm water is a mixture of FF and KO water masses and is warmer in winter than in summer. The authors find that seasonal differences in pathways double the fraction of FF particles in winter, causing the seasonal warming and salinification. Seasonal temperature variations at the upstream sections (FF and KO) have a negligible impact on temperature variations near the fjord. Successful monitoring of heat flux to the fjord therefore needs to take place close to the fjord and cannot be inferred from upstream conditions.

1. Introduction

The Greenland Ice Sheet (GIS) has been losing mass at an accelerating rate over the past two decades (IPCC 2013; Shepherd et al. 2012; Velicogna and Wahr 2013; Groh et al. 2014; Khan et al. 2015). A quadrupling of the loss over this period has increased its current sea level rise contribution to 25% of the total (Straneo and Heimbach 2013; Straneo and Cenedese 2015), with a significant sea level fingerprint in remote locations (Brunnabend et al. 2015; Rietbroek et al. 2016). GIS meltwater impacts the local ocean circulation and may in the future also affect the global ocean circulation through its impact on the Labrador Sea surface salinity, convection, and thereby the Atlantic meridional overturning circulation (Rahmstorf et al. 2015; Boning et al. 2016).

The striking simultaneous retreat of the Greenland glaciers has pointed toward environmental causes rather than (only) internal glacier dynamics (Luckman et al. 2006; Murray et al. 2010; Seale et al. 2011; Straneo et al. 2013). Next to atmospheric warming due to climate change, intrusion of warm-water masses into the Greenland fjords and a possible connection to the changes in the heat content in the lower latitudes have been proposed as an important factor (Holland et al. 2008; Christoffersen et al. 2012; Straneo and Heimbach 2013). The consequences of warm ocean water intrusion include undercutting of the glacial front (Hanna et al. 2009; Thomas et al. 2009) and a reduction of the sea ice cover, which in turn leads to higher atmospheric temperatures through a lowered albedo and potentially destabilization of ice melange on the calving front (Seale et al. 2011).

About half of the increased GIS mass loss is attributed to acceleration of the southeastern and western outlet glaciers (van den Broeke et al. 2009; Rignot et al. 2010; Straneo et al. 2013; Velicogna and Wahr 2013), of which Kangerdlugssuaq Glacier (KG) is the third largest contributor (Enderlin et al. 2014). KG underwent a major

Corresponding author: Renske Gelderloos, rgelder2@jhu.edu

DOI: 10.1175/JPO-D-16-0202.1

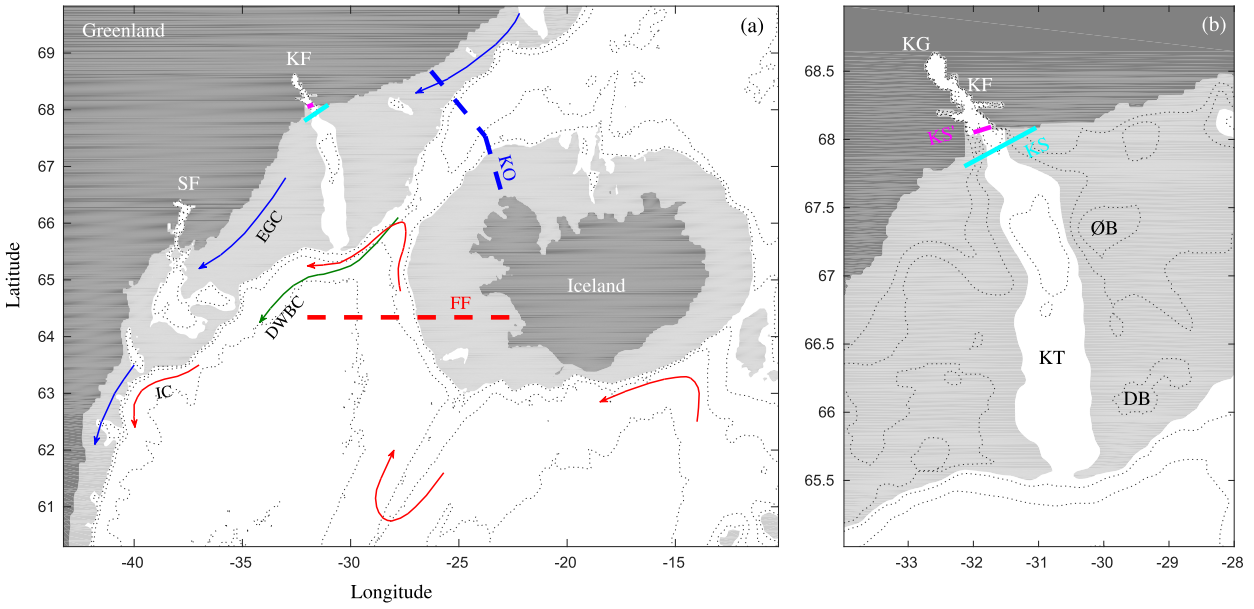

FIG. 1. (a) Model domain for the simulations. Depth contours have been drawn at 3000-, 2000-, 1000-, 500-, 400-, and 0-m depth. The shelf region shallower than 400-m depth is shaded light gray; dark gray is land. The blue and red dashed lines are the transects used in section 3, the cyan line is where the particles are released, and the magenta line in the fjord mouth is the KS′ CTD section used for model validation in section 2b. The colored arrows roughly indicate the pathways of the main currents. (EGC = East Greenland Current. IC = Irminger Current. DWBC = deep western boundary current. KO = Kögur section. FF = Faxaflói section. KF = Kangerdlugssuaq Fjord. SF = Sermilik Fjord.) (b) Close up of the Kangerdlugssuaq Glacier–Fjord–Trough area. Shading and depth contours are the same as in (a), with the 200- and 300-m isobaths added to bring out bathymetric features on the shelf. (KS = Kangerdlugssuaq section. KS′ = CTD line used for validation. KG = Kangerdlugssuaq Glacier. KF = Kangerdlugssuaq Fjord. KT = Kangerdlugssuaq Trough. ØB = Øst Bank. DB = Dohrn Bank.)

thinning of more than 100 m after 2003, and the records of glacier front positions and elevation suggest a complicated behavior that is not always captured by ice sheet models (Khan et al. 2014). The interaction between glaciers and the adjacent ocean is complicated, however, and depends on local and poorly understood factors such as fjord dynamics and buoyant plumes at the glacier–ocean interface (Straneo and Cenedese 2015).

Some key unknowns include the pathways of warm waters to the glacial fjords and the attendant hydrographic variability. Located just south of Denmark Strait, Kangerdlugssuaq Fjord (KF) is positioned at a confluence of ocean currents (Fig. 1). On the shelf, the East Greenland Current (EGC) carries cold and fresh water from the Arctic (Rudels et al. 2002; Sutherland and Pickart 2008). At the shelf break, the warm and saline Irminger Current carries water of subtropical North Atlantic origin, which is slightly denser than the freshwater on the shelf (e.g., Rudels et al. 2002). At greater depth, dense waters are found, formed by intense mixing of cascading Denmark Strait Overflow Water (DSOW) with the surrounding water masses (Price and Baringer 1994; Koszalka et al. 2013) and continuing onward in the deep western boundary current.

Although the general pattern of the regional ocean circulation in this area is well established (e.g., Rudels et al. 2002), very little is known about the interaction between the deep ocean and the shelf and seasonal variability therein. The confluence of ocean currents, combined with sea ice and a complicated bathymetry, make this a difficult area to observe. A compilation of 2004–10 summertime sealborne temperature data (Sutherland et al. 2013) showed that the cold EGC water is clearly visible above 150-m depth on the shelf. Atlantic-origin water is generally located seawards of the shelf, but upstream of Kangerdlugssuaq Trough (KT) it appears on the shelf. In addition to the summertime survey, the seasonal variability near Sermilik Fjord (downstream of Kangerdlugssuaq; Fig. 1) was also studied in that paper. While the deeper waters were warm year-round, in some locations the water shallower than 200 m was warm in summer and fall and cold in winter and spring. Because this seasonality was location dependent, Sutherland et al. (2013) hypothesized that variations in Irminger Current pathways could be responsible.

In situ observations inside Kangerdlugssuaq Fjord are limited to a few synoptic summertime surveys (Azetsu-Scott and Tan 1997; Christoffersen et al. 2012; Sutherland

et al. 2014; Inall et al. 2014) and one wintertime mooring (Jackson et al. 2014). These observations have confirmed the presence of warm water in the fjord, but some important questions remain: Where did this warm water come from, where and how did it cross the continental shelf, where did the water obtain its heat, and is there any seasonal variability in the heat delivery, and, as a consequence, how representative are summertime observations for annual-mean conditions?

The aim of this study is to address these questions. We address them using a year-long simulation of a very high-resolution regional model in combination with a Lagrangian particle-tracking tool. Based on in situ observations and knowledge of the regional circulation (Fig. 1), three potential sources of warm water have been identified: 1) warm Polar Surface Water (PSWw) is carried by the fresh EGC and has gained heat from interaction with the solar-warmed top layer on its way south, 2) warm and saline Atlantic Water (AW) is brought in by the Irminger Current at intermediate depths, and 3) DSOW is the dense water found at the bottom of the fjord, underneath the AW. By tracing the origin of the water that enters Kangerdlugssuaq Fjord in our model, we can form a kinematic picture of the time-varying water pathways. The focus of this manuscript is on identifying these pathways and on the impacts of changing pathways on the warm-water delivery to the fjord entrance; the mechanisms that would cause these pathways to be different, which could include the presence of sea ice, different local as well as remote wind conditions, and thermohaline forcing at the surface and internal ocean dynamics, are beyond the scope of the present study. Throughout the manuscript, we will refer to the differences between the summer and winter of the 2007/08 year as seasonal variability. As the seasonal cycle is much larger than interannual trends, other years may show quantitatively, but probably not qualitatively, different results.

A description of the ocean model setup and the Lagrangian particle-tracking algorithm are given in section 2. This section also covers model validation, a description of seasonal variability in the model, and a description of the setup of the particle-tracking simulations. Section 3 explores the particle pathways to the fjord and their seasonal dependence. In section 4, along-path water mass transformation is investigated. The results are summarized in section 5.

2. Methods

a. Ocean circulation and sea ice model

For a detailed representation of the circulation in this area, a regional ocean and sea ice model of the Irminger Sea and adjacent Greenland Shelf (Fig. 1) was created using the MITgcm (Marshall et al. 1997). The configuration builds upon previous setups (Magaldi et al. 2011; Koszalka et al. 2013; von Appen et al. 2014), which realistically captured the surface circulation, dense water transport, and the structure and transport through characteristic synoptic sections. To study the circulation in the vicinity of KF, several improvements were implemented as described below.

The nominal horizontal resolution is 2 km, and the layer thickness varies from 2 m near the surface to 15 m below 110-m depth. The model was run in hydrostatic mode for the period 1 June 2007 to 31 May 2008, after an initial 17-month spinup, as described in Magaldi et al. (2011). During the simulation, sea surface temperatures were relaxed on a 5-day time scale to the Operational Sea Surface Temperature and Sea Ice Analysis (OSTIA) product (Donlon et al. 2012). Surface forcings are based on ERA-Interim reanalysis fields (Dee et al. 2011). This product has been previously shown to adequately represent the scale and strength of winds in the region of interest (Harden et al. 2011) and to resolve high-frequency, down-slope wind events that influence the sea ice conditions in southeast Greenland fjords (Oltmanns et al. 2014). A further improvement is the inclusion of ship- and sealborne measurements of bathymetry (Sutherland et al. 2013), which improves the representation of the shelf circulation.

At the three open boundaries, velocities and tracer values are prescribed from a global HYCOM simulation (Chassignet et al. 2009), while Greenland forms a naturally closed boundary at the west side of the domain. A no-slip boundary condition is used for both the bottom and sidewalls. The KPP scheme with a background vertical viscosity of $10^{-5}\,m^2\,s^{-1}$ is used (Large et al. 1994), and the Leith scheme for horizontal viscosity is applied (Leith 1967).

The ocean model is coupled to a viscous plastic dynamic/thermodynamic sea ice model, as described in Menemenlis et al. (2005), Losch et al. (2010), and Heimbach et al. (2010). Sea ice and snow thicknesses, sea ice fraction, and salinity are all advected by ice velocities via a second-order scheme with flux limiters. Salt rejected during sea ice formation is treated using the subgrid-scale salt plume parameterization of Nguyen et al. (2009). Open boundary conditions for all sea ice variables are obtained from the 1/8° Towards an Operational Prediction System for the North Atlantic European Coastal Zone, version 4 (TOPAZv4), monthly reanalysis data (Sakov et al. 2012). The interior sea ice fields are nudged to the TOPAZ reanalysis values within 20 points of the grid edge. The nudging time scale is 1 day at the boundaries and linearly

increases toward the interior to reach the maximum value of 10 days. There is no spinup for sea ice; the initial sea ice conditions are derived from the TOPAZv4 reanalysis data for May 2007.

b. *Mean hydrographic properties at the control sections*

The general ocean circulation, volume fluxes, and water properties in the ocean model have been compared to observations at the standard sections along the boundary current system in the Irminger Basin with a very good agreement (Denmark Strait, Spill Jet, Angmagssalik; see Magaldi et al. 2011; Koszalka et al. 2013), and we therefore focus here on the hydrographic properties at the control sections used in this study. Particle trajectories are traced back from the KF entrance to two upstream control sections, chosen to coincide with known hydrographic repeat sections (Fig. 1). Between Iceland and Greenland, just upstream of Denmark Strait, the Kögur section (KO) captures water masses flowing in from the Arctic and Nordic Seas. The Faxaflói section (FF) west of Iceland captures the warm and saline water of subtropical origin in the Irminger Current. All available high-resolution conductivity–temperature–depth (CTD) observations in this area were extracted from the World Ocean Database (Boyer et al. 2013), and all stations within 5 km of the respective hydrographic sections were mapped onto the sections and compared to the annual-mean hydrography from the model (Figs. 2, 3). The FF composite contains 440 stations taken between 1996 and 2011; the KO composite is composed of 314 stations taken between 1982 and 2011.

The FF comparison in Fig. 2 shows excellent agreement in the potential temperature (θ) structure (Figs. 2a,c) and a slightly less saline top 500 m in the model compared to observations (Figs. 2b,d). The difference is small and likely because most observations were taken in summer, when the stratification is stronger. The KO comparison in Fig. 3 shows again excellent agreement for potential temperature (Figs. 3a,c), with a small difference in structure on the Iceland side (right-hand side in the figure) of the section. The KO salinity (S) comparison (Figs. 3b,d) shows that the model is biased salty in the top 100 m. One might expect that this is in fact a bias in the (mostly summertime) observations, as sea ice melt reduces the near-surface salinity. However, the model summer mean is also too salty (Fig. 3f), and we have verified that this bias is inherited from a too salty EGC in the boundary conditions. The subsurface, however, shows very good agreement.

The upstream control sections, which can be directly compared with observations, thus show realistic θ–S properties. The particle release section [Kangerdlugssuaq section (KS), cyan line in Fig. 1] was chosen outside of the fjord because the model resolution is not sufficiently high to capture the details of the fjord circulation. Observations at this section are not available, but the World Ocean Database does contain CTD observations on a section just north of KS from September 2007, which we will refer to as KS′ (magenta line in Fig. 1) and use for comparison with model data on this same section. Because of the limited amount of data, comparison is not performed on the annual mean but on the late September fields.

Figure 4 shows the potential temperature (top), salinity (middle), and potential density (bottom) from observations on 28 September 2007 (right) and its model equivalent averaged from 5 days before to 5 days after this date to eliminate short-term variability (left). In the bottom panels, the water masses according to Inall et al. (2014) are overlaid in colored dashed contour lines. The water mass comparison shows that the DSOW, modified Atlantic Water (AWm), and PSWw are all present and found in the same depth ranges. The cold layer of PSW is somewhat deeper in the model than in observations. Furthermore, as glacial melt and runoff were not included in the model simulation, the very fresh surface water found in observations is absent in the model fields. The somewhat lower model salinities in the upper 200 m are furthermore consistent with the salinity bias found in the EGC at the Kögur section. The subsurface hydrographic properties are in good agreement.

The above model validation confirmed that the model reproduces the mean hydrographic properties from observations well. In the remainder of this manuscript, we will therefore focus on the model output fields.

c. *Seasonal variability at the control sections*

The central question in this study concerns the differences in pathways between the summer (ice free) and winter (ice covered) seasons. We therefore split the model output into two 5-month periods: July–November (JASON), when the area around KF/KT is ice free, and January–May (JFMAM), when the shelf region is covered in sea ice.

At the particle release site KS (Fig. 5), the water below 200-m depth is warmer and saltier in winter than in summer. The top 200 m, on the other hand, is colder and slightly fresher. As a result, the water column in winter is more strongly stratified.

The seasonal fields at the upstream FF section (Figs. 2e–h) show similar variability, though much less pronounced in the subsurface: the top circa 500 m is about 1°C warmer in the summer season, but below this depth the water is slightly warmer in winter. The salinity in the lower water column changes little over the year, but the upper 500 m is well mixed in winter, thereby

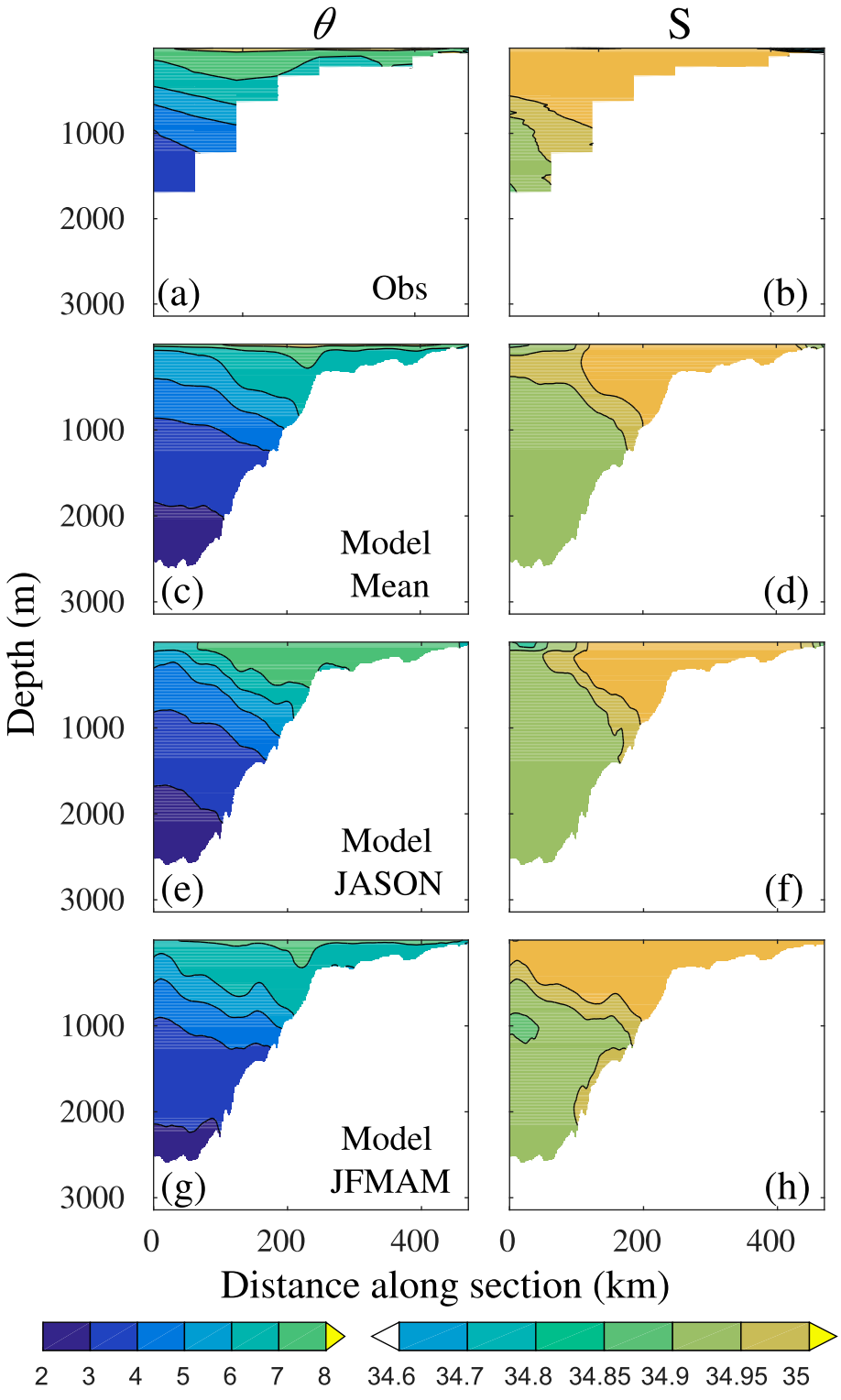

FIG. 2. (left) Potential temperature (°C) and (right) salinity (psu) along FF (red dashed line in Fig. 1). (a),(b) Composite of high-resolution CTD observations; (c),(d) model annual-mean hydrography; (e),(f) model mean over July–November period; and (g),(h) model mean over January–May period.

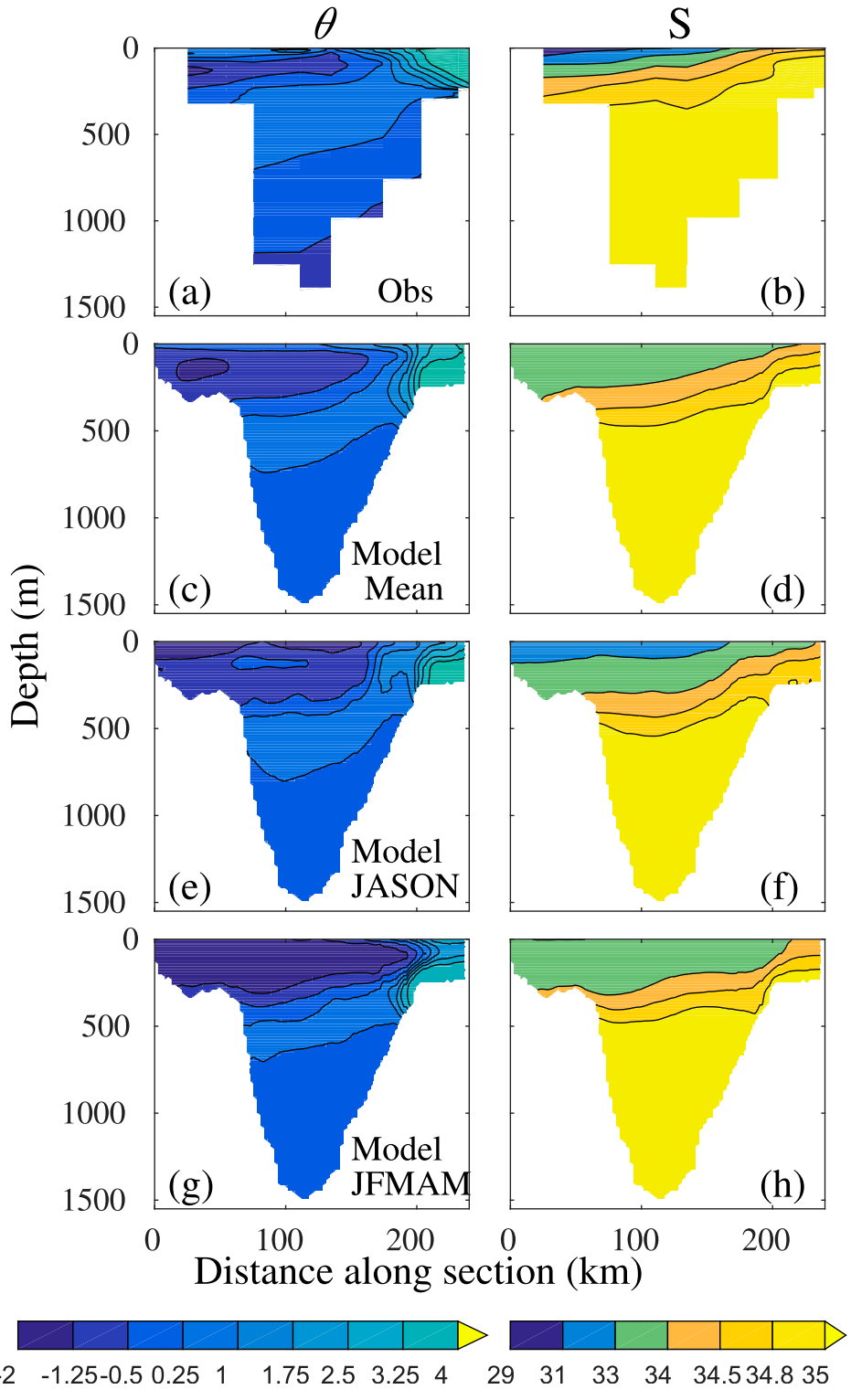

FIG. 3. As in Fig. 2, but for the KO (blue dashed line in Fig. 1). Note that the color bars are different from those in Fig. 2.

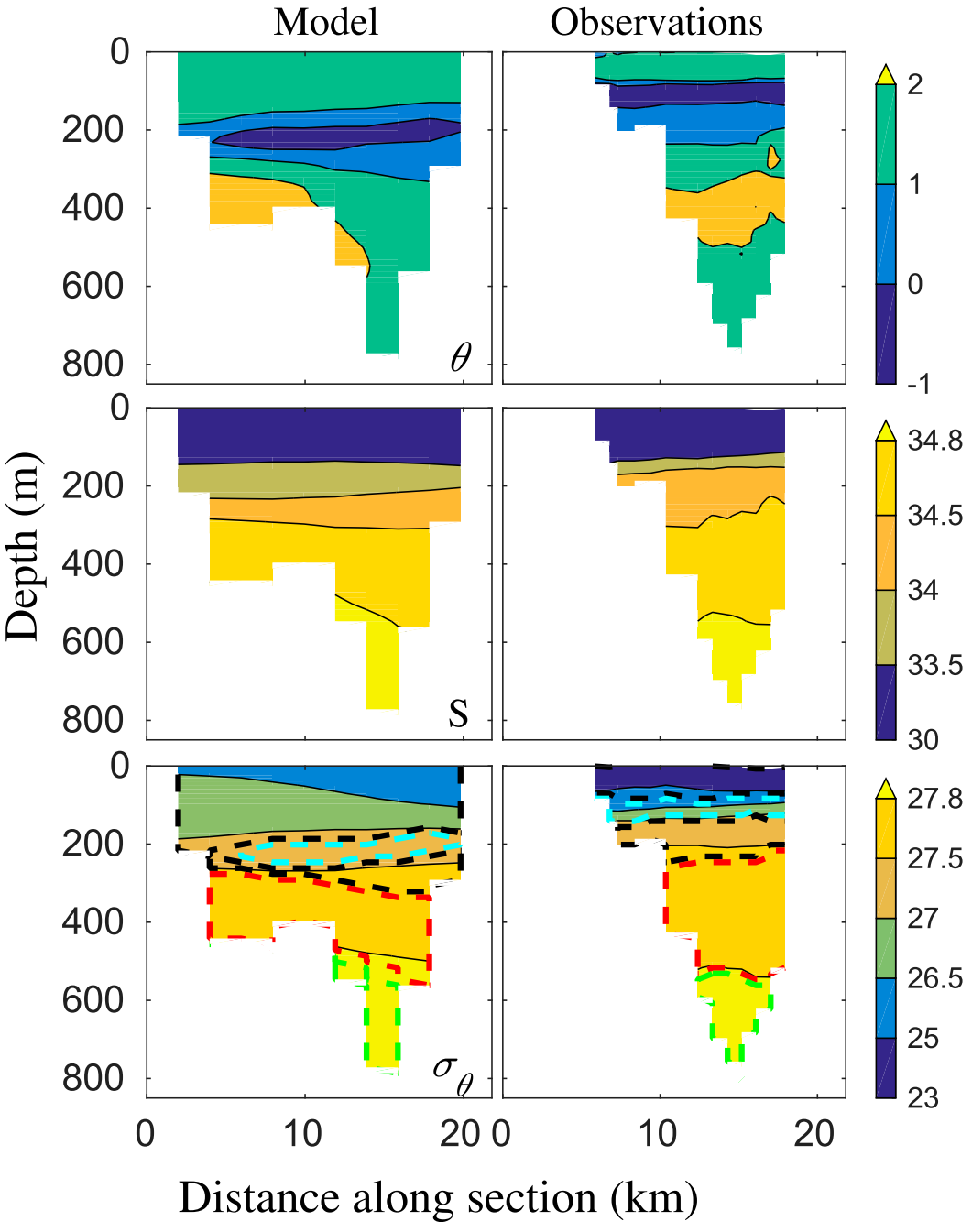

FIG. 4. (top) Potential temperature (°C), (middle) salinity (psu), and (bottom) potential density (kg m^{-3}) along the KS′ section (magenta line in Fig. 1). Observations (right) were taken on 28 Sep 2007. Model fields (left) are an average over the 5 days before to 5 days after this date. The colored dashed contours in the bottom panels indicate water masses: warm Polar Surface Water (black), Polar Surface Water (cyan), modified Atlantic Water (red), and Denmark Strait Overflow Water (green).

reducing the salinity on the Iceland shelf and increasing it on the slope and farther offshore. In contrast to KS, stratification is therefore weaker in winter at FF. Variability at the other upstream section (KO; Figs. 3e–h) is similar to that at FF. The top 500 m is warmer and more stratified in summer than in winter. Below this depth the θ–S characteristics are very similar.

To study to what extent θ–S properties are inherited from upstream conditions, and how the path taken to reach the fjord entrance affects changes in these

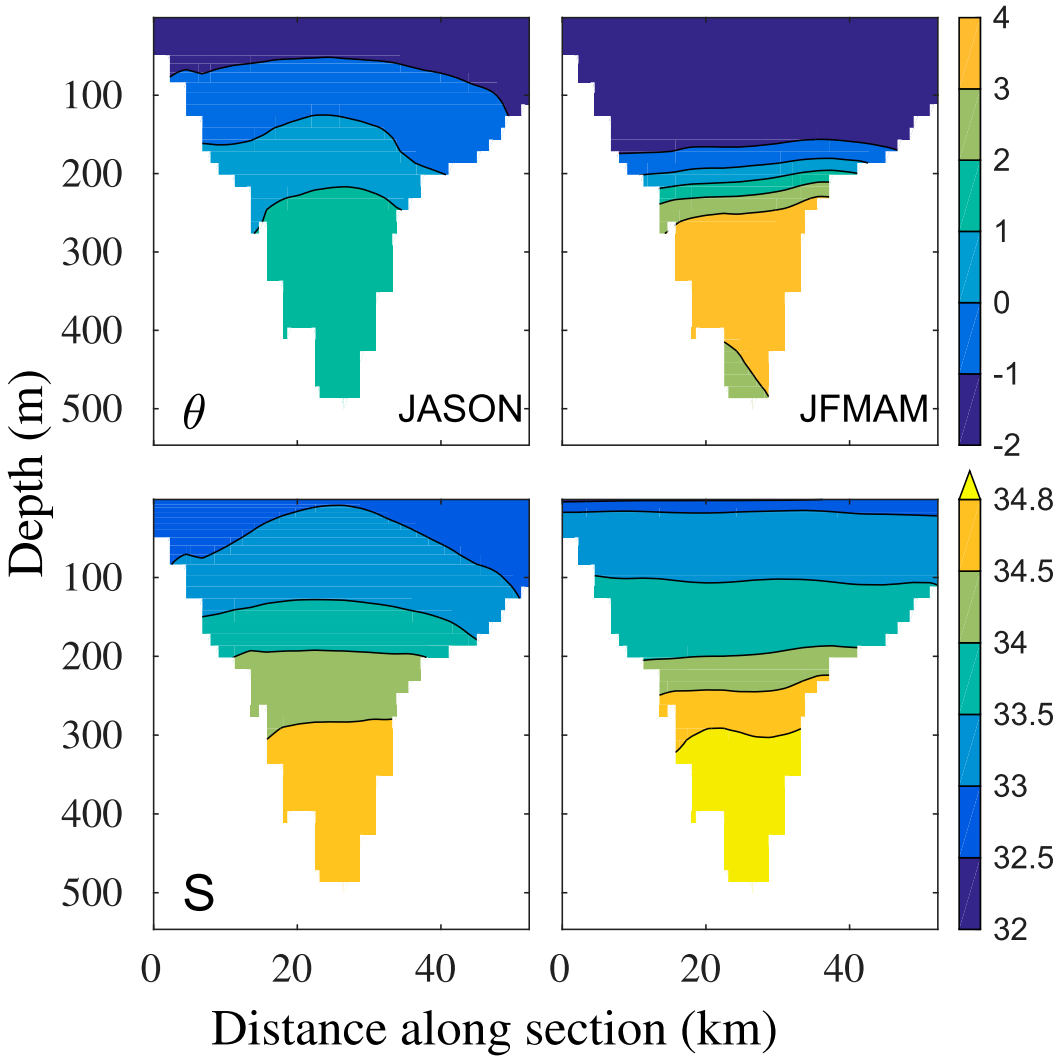

FIG. 5. Seasonal-mean sections at the particle release section (cyan line in Fig. 1) for potential temperature (°C, top) and salinity (psu, bottom): (left) JASON and (right) JFMAM.

characteristics, Lagrangian particles are released at KS and traced back to either FF or KO. The remainder of this section discusses details of the Lagrangian particle-tracking algorithm and the specific simulation setup choices used in this study.

d. Lagrangian particle-tracking model

The numerical particle trajectories are simulated offline using a particle-tracking algorithm from Koszalka et al. (2013; see also Gelderloos et al. 2016). The discrete MATLAB software employs a trapezoidal solver with a second-order predictor and third-order corrector scheme. The particles are advanced with the three-dimensional model velocity linearly interpolated on instantaneous particle positions. For the boundary conditions, the velocity component normal to the bathymetric boundary is zero so that particles slide along the bottom and walls of the domain. There is no explicit diffusion in the particle code. The tracer fields are linearly interpolated onto the particle positions to obtain time series of salinity and temperature.

The particle-tracking algorithm uses 6-hourly snapshots from the ocean model as input. We conducted a sensitivity study and found that a 6-h time interval for the ocean model output is sufficient to resolve the flow variability on the east Greenland shelf and attain a convergence of ensemble particle position and travel time statistics (I. M. Koszalka et al. 2017, unpublished manuscript).

e. Setup of the simulations

A total of 1274 particles are seeded twice a day at the KS section near the fjord entrance. They are spaced

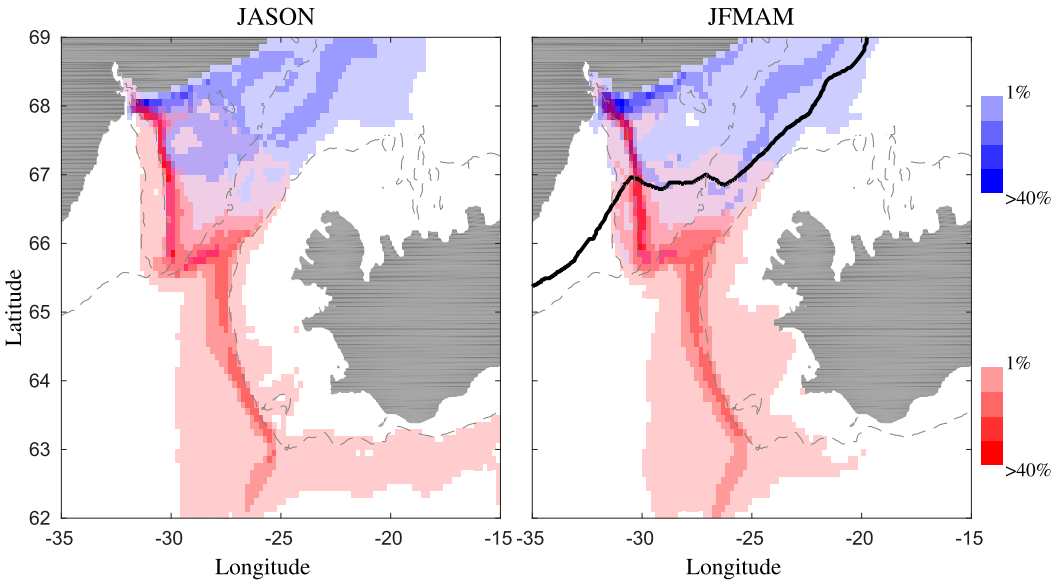

FIG. 6. Particles trajectories per season. The shading indicates the fraction of particle trajectories per control section reaching that location in the model domain. Only values exceeding 1% are shaded. Color coding is the same as in Fig. 1. The 400-m isobath is shown as the dashed gray contour. The black solid contour represents the offshore edge of the area exceeding 50% sea ice coverage. Note that the pathways are three-dimensional but are projected onto the horizontal plane in this figure.

500 m in the horizontal and 25 m in the vertical and occupy the 50–500-m depth range. Particles are seeded in May and November (the last months of our winter and summer seasons) with 61 releases in each month. The total number of particles tracked is thus about 155 000.

The particles are tracked backward in time for 5 months. A year-long sensitivity study with 3822 particles showed that over 80% of the particles that reach either the KO or FF section (83% of the total) do so within this period, 15% of the particles are killed because they come within 5 m of the surface, and less than 2% remain in the subsurface but do not reach either section within a year. Important to note is that the statistics on θ–S transformation from KO/FF to KS do not change for simulations of 4 months or longer. Only particles that could be traced back to either the KO or the FF section are included in the analysis. The two sections represent distinct sources, as only a negligible fraction ($\ll$1%) of KO particles originated in the Irminger Basin and FF particles originated in the Nordic Seas.

3. Preferred pathways

a. A horizontal view

The pathways followed by particles approaching KF are visualized in Fig. 6. The figure shows the likelihood that an area will be visited by a particle in the given season. Although some significant differences between the seasons are clear, parts of the pathways are common to both seasons and notably influenced by bathymetry. In particular, the KT steers the flow toward the fjord entrance.

The KO particles (blue shading) show the largest seasonal variability. A coastal route appears in both summer and winter, but a second (offshore) pathway crosses onto the shelf around 67.5°N in summer, while it follows the continental slope and takes the long way around Dohrn Bank and into KT in winter. Given the fact that sea ice overlies the summertime crossing location onto the shelf (Fig. 6), the presence or absence of the sea ice could play a role in changing the preferred route.

The FF particles (red shading) exhibit less variation with season. They generally follow the rim of the Irminger Basin into the Denmark Strait, as previously described by Rudels et al. (2002), and then return to the Irminger Basin and into the KT. A small fraction of the FF particles follow a route northward through Denmark Strait and then onto the shelf in summer, but like the KO particles, in the winter months trajectories are restricted to the KT.

The seasonal difference in preferred routes leads to different typical transit times from the upstream control sections to KS (Fig. 7). Both source waters take longer to reach the fjord in winter than in summer: the median transit time for FF particles increases from 56 to 73 days, while the median transit time for KO particles doubles from 44 to 97 days. In summer, the fastest route is thus from the KO section, while in winter the FF particles reach the fjord first. This is reflected in the fractionation

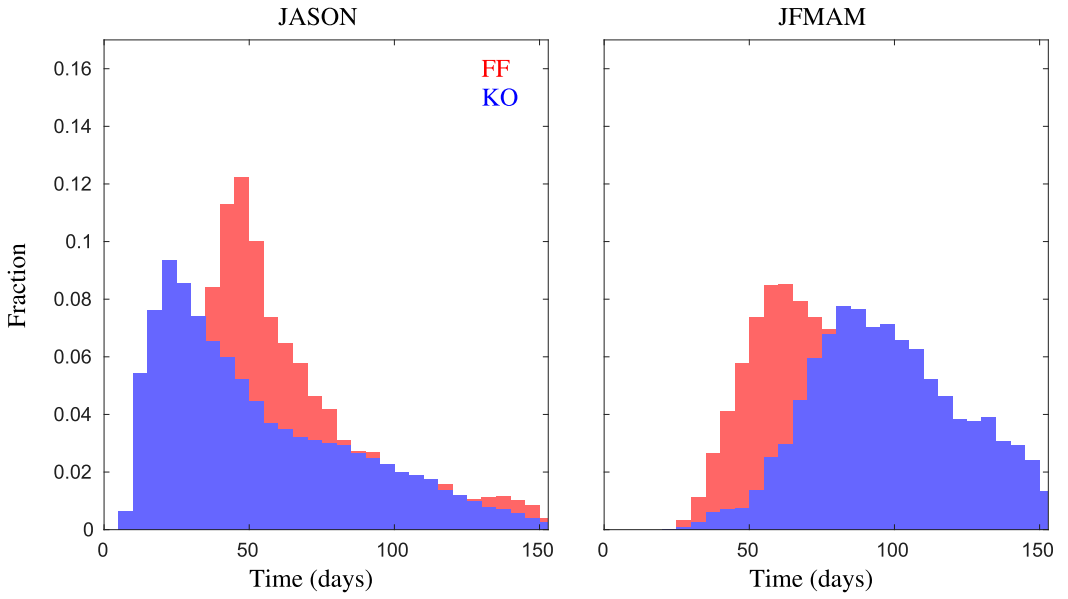

FIG. 7. Transit time distributions in (left) summer and (right) winter. Color coding is the same as in Fig. 1.

between the two sources (Fig. 8). In summer, 9% of particles originate from FF, while in winter this fraction doubles to 20%.

b. *Vertical distribution in the water column*

The observations and model sections in Fig. 4 showed that the different water masses typically occupy a certain depth range at KS: PSWw at the top, AWm at middepth, and DSOW in the deepest part of the water column. Figure 8 (solid lines) shows how many particles (as a fraction of the total traced number in that season) from a certain control section arrive at a certain depth at KS. It shows that the observed water mass distribution roughly corresponds to the water masses from our upstream control sections: the FF-origin particles are mostly found in the 200–400-m depth range, while the KO particles occupy the top 200 m and the lowest part of the water column.

While the qualitative pattern is similar in winter and summer, the stratification is much more pronounced in winter. In summer, both the FF and KO particles are more spread out over the water column, while in winter KO particles seem to avoid the central depth range. These findings are in line with the increased stratification in winter at KS (Fig. 5).

4. Seasonal variations in θ–S transformation

The significantly larger volume fraction of FF-origin particles in winter (Fig. 8) could explain the warmer and more saline subsurface at KS in that season (Fig. 5). To confirm this hypothesis, we now look at the θ–S properties of the water particles as a measure for the heat and salt they carry to the fjord entrance.

a. *Particle θ–S properties at the control sections*

Figures 9a and 9b show the θ–S transformation of the particles from their upstream control sections to the KS section at the fjord entrance in a θ–S diagram. The particles that travel from the FF to the KS section (red to magenta) start out at roughly the same salinity in both seasons, but summer particles have a 0.5°C higher temperatures on average. They cool and freshen along their trajectories in both seasons, but nearly 2°C and 0.25 psu more in summer. The particles that travel from the KO to the KS section (blue to green) show a different behavior. In summer, their average properties hardly change, that is, the widespread cooling of the particles in the upper layers in the latter months of this season is offset by mixing with the warmer water in the Irminger Basin. Cooling in winter is much stronger, and therefore the mean temperature, dominated by the larger number of particles in the upper part of the water column (Fig. 8), goes down in this season. The mean freshening occurs because the sea ice is starting to melt in the latter part of this period.

The water mass transformation of FF particles seems peculiar, as the particles are warmer at the FF section in summer than in winter but cool so much in summer that the average potential temperature is lower by the time they reach the KS section than it is in winter. So, the faster pathway from the FF section in winter appears to

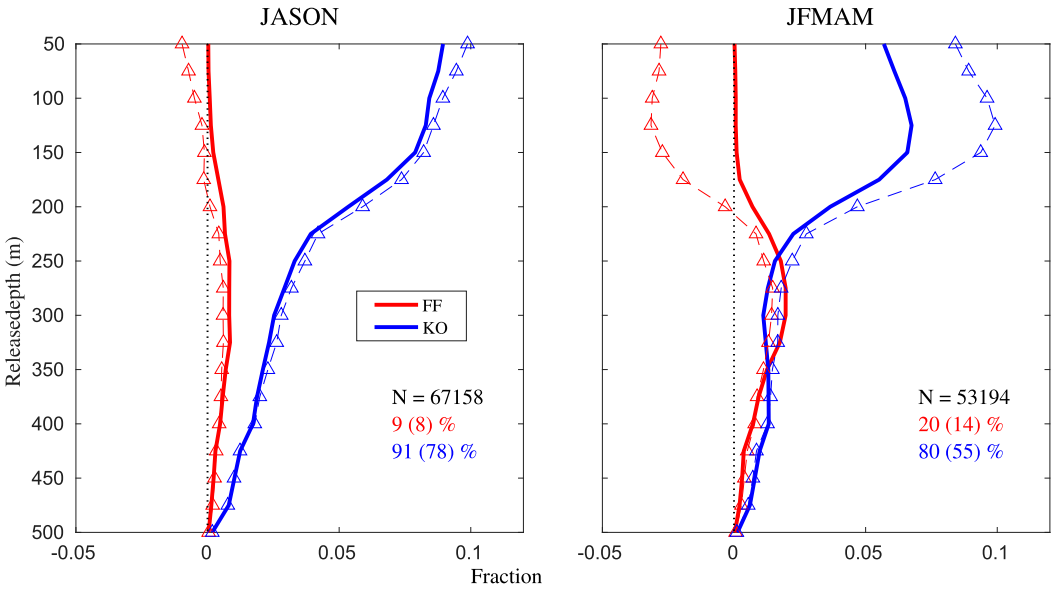

FIG. 8. The fraction of particles from each upstream control section of the total number of particles in the season as a function of origin section and the depth that they were released at Kangerdlugssuaq section (solid lines). The total number of particles per season (N) is noted in each panel. The colored percentages indicate the fraction of this total over the two origin sections for that season; the parenthetical numbers give the percentage of the total number of particles released for completeness. The dashed lines are the required fractions to obtain the water properties at Kangerdlugssuaq section by mixing of FF and KO water masses. The black dotted line is the zero fraction grid line.

facilitate a doubling of the fraction of FF particles in that season, causing the water to be warmer and more saline (Figs. 9a,b).

b. *Localization of mixing*

A plausible cause of enhanced cooling and freshening of the FF particles in summer is increased mixing with the colder and fresher water masses from the KO section. The pathways in Fig. 6 suggest that the water masses come into contact with one another and are able to exchange properties. The Lagrangian framework uniquely enables spatial mapping of these property changes along particle paths. The rate of change of temperature was extracted from the two particle sets, spatially binned, and then averaged. Figure 10 shows in red shading the regions where FF particles lose heat at a rate larger than $0.02^{\circ}\mathrm{C\,day^{-1}}$ and in blue shading the regions where KO particles gain heat at a rate larger than $0.02^{\circ}\mathrm{C\,day^{-1}}$. The figure shows that the regions where KO particles gain heat coincide with the regions where FF particles lose heat, in particular south of Denmark Strait in the Dohrn Bank area, which is in line with previous work by Koszalka et al. (2013).

c. *Seasonal variability in mixing rates*

To quantify the amount of en route mixing, we make two assumptions: First, below 200-m depth (where the FF particles are found at KS), there are no other sources of heat and salt than water coming through the KO and FF sections, that is, the impact of ocean–atmosphere exchange on the water properties at depth are minimal. Second, the θ–S characteristics of the particles from KO/FF are representative of the water mass properties of water going through these sections (cf. Figs. 2e–h and 3e–h with Fig. 9). With these assumptions, the water mass properties at KS are a simple linear function of the upstream properties and mixing ratios, as calculated from mixing the FF and KO water masses along a straight line in θ–S space (Gill 1982) using the volume ratios based on the particle fractions

$$\begin{bmatrix}\theta_{\mathrm{KS}}\\ S_{\mathrm{KS}}\end{bmatrix} = f_{V,\mathrm{FF}}\begin{bmatrix}\theta_{\mathrm{FF}}\\ S_{\mathrm{FF}}\end{bmatrix} + f_{V,\mathrm{KO}}\begin{bmatrix}\theta_{\mathrm{KO}}\\ S_{\mathrm{KO}}\end{bmatrix}, \tag{1}$$

where f_V is the volume fraction of the water mass, according to

$$f_{V,\mathrm{FF}}(z_k,\mathrm{SEAS}) = \frac{f_{\mathrm{FF}}(z_k,\mathrm{SEAS})}{f_{\mathrm{FF}}(z_k,\mathrm{SEAS}) + f_{\mathrm{KO}}(z_k,\mathrm{SEAS})},$$

where $f_{\mathrm{FF}}(z_k, \mathrm{SEAS})$ are the fractions from Fig. 8 for discrete release depth z_k and season SEAS. The quantities θ and S are the potential temperature and salinity at the control sections. All variables are a function of release depth and season.

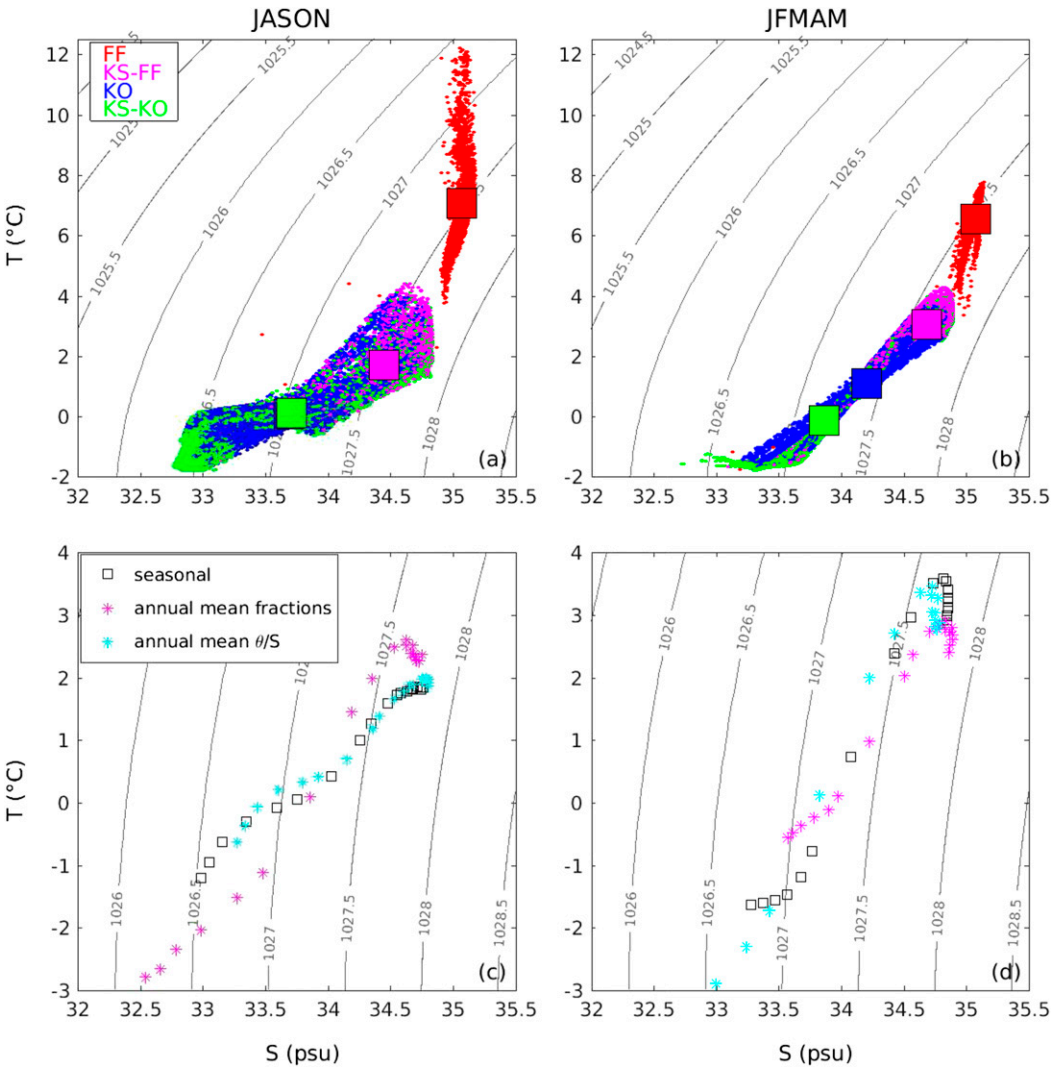

FIG. 9. (a),(b) Temperature–salinity diagrams for (left) JASON and (right) JFMAM particle trajectories. The dots are the θ–S characteristics at the control sections. Red dots indicate properties at Faxaflói, magenta dots indicate the θ–S values of these same particles at Kangerdlugssuaq section, blue dots represent the θ–S properties at Kögur, and green dots indicate their transformed values at the Kangerdlugssuaq section. The squares are the mean values over all particles in that subset. (c),(d) Comparison between mixing model results [Eq. (1)] using seasonally varying values (black squares), annual-mean θ–S properties at the upstream control sections (cyan asterisks) and annual-mean volume fractions (magenta asterisks).

Instead of solving for S_{KS} and θ_{KS}, we use the values from the ocean model (Fig. 5) and solve for the required volume fractions to produce these hydrographic properties (dashed line with triangles in Fig. 8). As expected, the linear mixing model performs poorly in the upper 200 m, especially in winter, where nearly all particles originate from the KO section and water properties changes are determined largely by atmosphere–ocean and/or ice–ocean interaction. Below 200 m, however, the mixing model predicts the ocean model θ–S properties very well.

Now that we have established that the linear mixing model is appropriate for the depth range at KS that becomes warmer and saltier in the winter season, we will use this model to determine whether the seasonal variability is determined mostly by the seasonal variability of the θ–S properties of the upstream control sections or by seasonal variability in mixing of the water masses.

First, we make slight adjustments to the volume fractions so that the calculated θ–S properties exactly match the ocean model values (above 200 m, the adjustment is large, but we include these values for completeness). The

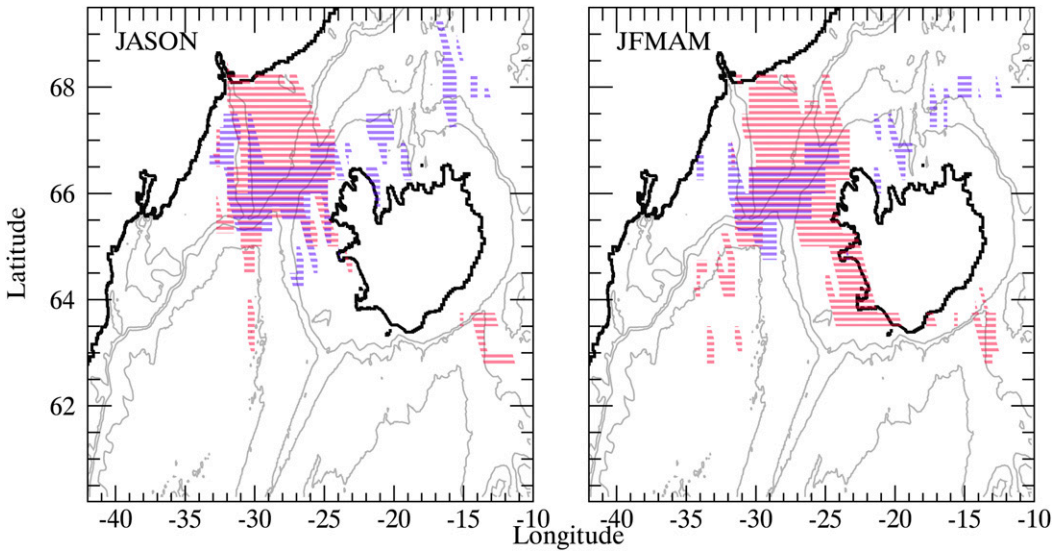

FIG. 10. Comparison of regions where FF particles lose heat at a rate exceeding 0.02°C day^{-1} (red) and where KO particles gain heat exceeding the same rate (blue).

θ–S properties thus found are plotted in Figs. 9c and 9d as the black squares. Second, we repeat the calculation, but instead of using seasonally varying values for the water properties θ_{FF}, S_{FF}, θ_{KO}, and S_{KO}, we use their annual-mean values. The hypothetical θ_{KS} and S_{KS} calculated are plotted as the cyan asterisks in Figs. 9c and 9d. In the top layers (cold/fresh corner of the θ–S diagram), the models match poorly as expected. In the lower part of the water column, however, there is a surprisingly good agreement. Third, the hydrographic properties are allowed to vary with season, but the volume fractions are held constant at their annual-mean value. The resulting θ_{KS} and S_{KS} are the magenta symbols in Figs. 9c and 9d. Clearly, not incorporating seasonal variability in mixing rates yields large deviations from the model θ–S properties at KS, while ignoring seasonal variations in upstream θ–S properties has very little effect.

5. Summary and discussion

In this study, the pathways and along-path transformation of warm-water masses toward Kangerdlugssuaq Fjord were investigated in a Lagrangian framework using a very high-resolution model. Based on the water masses found near the fjord entrance, two sections were identified to distinguish between different regions of origin. They are the Kögur hydrographic repeat section (KO) between Iceland and Greenland, accounting for contributions of waters from the Nordic Seas, and the zonal Faxaflói hydrographic repeat section (FF) west of Iceland, covering water mass contributions from the Irminger Basin. Neutrally buoyant particles were seeded near the fjord entrance (KS section) and backtracked in the full 3D velocity field for a period of 5 months to identify the origin of the particles. Only particles that crossed at least one of the two sections of origin were analyzed.

The analysis showed that in the top 200 m of the water column the water almost exclusively originates from the KO section. FF particles are found between 200- and 400-m depth and form the main water mass there in winter. In the lowest part of the water column, the KO section is again the dominant source.

Both the pathways and properties of the water masses vary seasonally. In both seasons the FF particle trajectories follow the bathymetry into Kangerdlugssuaq Trough, while some go north through Denmark Strait and then across the shelf. In contrast to the results of Sutherland et al. (2013) for the shelf region around Sermilik Fjord, we do not find that FF water occupies the whole water column in summer but rather that the FF water mass is more spread out in summer and actually more dominant in the winter season. The differences between our results and those of Sutherland et al. (2014) are likely due to differences in the data distribution, in particular the tendency of seals to visit only certain regions (these more biologically productive), while the Lagrangian particles trace the flow pathways. The KO particles follow a coastal route year-round and a more offshore route that varies seasonally. It crosses the shelf in summer but follows the bathymetry around Dohrn Bank into Kangerdlugssuaq Trough in winter.

The seasonal differences in pathways are reflected in the particle travel times. In summer, the KO particles

are the first to arrive at the KS sections with a median travel time of 44 versus 56 days for FF particles. The longer, offshore KO route in winter doubles the travel time to 97 days, however, while FF particles only take 73 days, making the FF travel time the shortest in winter. With the KO particles taking a longer route in winter, the fraction of FF particles at KS doubles from 9% in summer to 20% in winter, causing a warmer and more saline water mass at KS in winter below 200-m depth.

Although the water mass properties at the control sections show a pronounced seasonal variability, the impact of these variations on the θ–S properties at KS is negligible compared to seasonal variations in the mixing fractions. For this reason, we conclude that in situ monitoring of the heat flux to Kangerdlugssuaq Fjord likely requires measurements close to the fjord, as seasonal variations in the upstream water mass properties are not inherited at the fjord entrance. Furthermore, although we cannot make firm statements on interannual variability based on a 1-yr simulation, we conjecture that long-term changes in upstream hydrographic conditions that are small compared to the seasonal cycle may be masked by variations in mixing rates. Possible indirect effects through changes in the circulation have, however, not been investigated in this study. Finally, interannual or decadal variations in the sea ice characteristics off east Greenland are likely important for variations in the offshore KO route in winter and thus likely impact interannual variability in mixing rates.

Acknowledgments. This work was supported by NSF Grants OCE-1433448 and OCE-1129895.

REFERENCES

Azetsu-Scott, K., and F. C. Tan, 1997: Oxygen isotope studies from Iceland to an east Greenland Fjord: Behaviour of glacial meltwater plume. *Mar. Chem.*, **56**, 239–251, doi:10.1016/S0304-4203(96)00078-3.

Boning, C. W., E. Behrens, A. Biastoch, K. Getzlaff, and J. L. Bamber, 2016: Emerging impact of Greenland meltwater on deepwater formation in the North Atlantic Ocean. *Nat. Geosci.*, **9**, 523–527, doi:10.1038/ngeo2740.

Boyer, T. P., and Coauthors, 2013: *World Ocean Database 2013*. NOAA Atlas NESDIS 72, 209 pp., doi:10.7289/V5NZ85MT.

Brunnabend, S.-E., J. Schröter, R. Rietbroek, and J. Kusche, 2015: Regional sea level change in response to ice mass loss in Greenland, the West Antarctic and Alaska. *J. Geophys. Res. Oceans*, **120**, 7316–7328, doi:10.1002/2015JC011244.

Chassignet, E. P., and Coauthors, 2009: US GODAE: Global ocean prediction with the Hybrid Coordinate Ocean Model (HYCOM). *Oceanography*, **22**, 64–75, doi:10.5670/oceanog.2009.39.

Christoffersen, P., M. O'Leary, J. H. van Angelen, and M. van den Broeke, 2012: Partitioning effect from ocean and atmosphere on the calving stability of Kangerdlugssuaq Glacier, east Greenland. *Ann. Glaciol.*, **53**, 249–256, doi:10.3189/2012AoG60A087.

Dee, D. P., and Coauthors, 2011: The ERA-Interim reanalysis: Configuration and performance of the data assimilation system. *Quart. J. Roy. Meteor. Soc.*, **137**, 553–597, doi:10.1002/qj.828.

Donlon, C. J., M. Martin, J. D. Stark, J. Roberts-Jones, E. Fiedler, and W. Wimmer, 2012: The Operational Sea Surface Temperature and Sea Ice Analysis (OSTIA). *Remote Sens. Environ.*, **116**, 140–158, doi:10.1016/j.rse.2010.10.017.

Enderlin, E. M., I. M. Howat, S. Jeong, M.-J. Noh, J. H. van Angelen, and M. R. van den Broeke, 2014: An improved mass budget for the Greenland Ice Sheet. *Geophys. Res. Lett.*, **41**, 866–872, doi:10.1002/2013GL059010.

Gelderloos, R., A. S. Szalay, T. W. N. Haine, and G. Lemson, 2016: A fast algorithm for neutrally-buoyant Lagrangian particles in numerical ocean modeling. *Proc. 2016 IEEE 12th Int. Conf. on e-Science*, Baltimore, MD, Institute of Electrical and Electronics Engineers, 381–388, doi:10.1109/eScience.2016.7870923.

Gill, A. E., 1982: *Atmosphere–Ocean Dynamics*. Academic Press, 662 pp.

Groh, A., H. Ewert, M. Fritsche, A. Rülke, R. Rosenau, M. Scheinert, and R. Dietrich, 2014: Assessing the current evolution of the Greenland Ice Sheet by means of satellite and ground-based observations. *Surv. Geophys.*, **35**, 1459–1480, doi:10.1007/s10712-014-9287-x.

Hanna, E., J. Cappelen, X. Fettweis, P. Huybrechts, A. Luckman, and M. H. Ribergaard, 2009: Hydrologic response of the Greenland Ice Sheet: The role of oceanographic warming. *Hydrol. Processes*, **23**, 7–30, doi:10.1002/hyp.7090.

Harden, B. E., I. A. Renfrew, and G. N. Petersen, 2011: A climatology of wintertime barrier winds off southeast Greenland. *J. Climate*, **24**, 4701–4717, doi:10.1175/2011JCLI4113.1.

Heimbach, P., D. Menemenlis, M. Losch, J.-M. Campin, and C. Hill, 2010: On the formulation of sea-ice models. Part 2: Lessons from multi-year adjoint sea-ice export sensitivities through the Canadian Arctic Archipelago. *Ocean Modell.*, **33**, 145–158, doi:10.1016/j.ocemod.2010.02.002.

Holland, D. M., R. H. Thomas, B. de Young, M. H. Ribergaard, and B. Lyberth, 2008: Acceleration of Jakobshavn Isbrae triggered by warm subsurface ocean waters. *Nat. Geosci.*, **1**, 659–664, doi:10.1038/ngeo316.

Inall, M. E., T. Murray, F. R. Cottier, K. Scharrer, T. J. Boyd, K. J. Heywood, and S. L. Bevan, 2014: Oceanic heat delivery via Kangerdlugssuaq Fjord to the south-east Greenland Ice Sheet. *J. Geophys. Res. Oceans*, **119**, 631–645, doi:10.1002/2013JC009295.

IPCC, 2013: *Climate Change 2013: The Physical Science Basis*. Cambridge University Press, 1535 pp.

Jackson, R. H., F. Straneo, and D. A. Sutherland, 2014: Externally forced fluctuations in ocean temperature at Greenland glaciers in non-summer months. *Nat. Geosci.*, **7**, 503–508, doi:10.1038/ngeo2186.

Khan, S. A., and Coauthors, 2014: Glacier dynamics at Helheim and Kangerdlugssuaq Glaciers, southeast Greenland, since the Little Ice Age. *Cryosphere*, **8**, 1497–1507, doi:10.5194/tc-8-1497-2014.

——, A. Aschwanden, A. A. Bjørk, J. Wahr, K. K. Kjeldsen, and K. H. Kjær, 2015: Greenland Ice Sheet mass balance: A review. *Rep. Prog. Phys.*, **78**, 046801, doi:10.1088/0034-4885/78/4/046801.

Koszalka, I. M., T. W. N. Haine, and M. G. Magaldi, 2013: Fates and travel times of Denmark Strait overflow water in the Irminger Basin. *J. Phys. Oceanogr.*, **43**, 2611–2628, doi:10.1175/JPO-D-13-023.1.

Large, W. G., J. C. McWilliams, and S. C. Doney, 1994: Oceanic vertical mixing: A review and a model with nonlocal boundary layer parameterization. *Rev. Geophys.*, **32**, 363–403, doi:10.1029/94RG01872.

Leith, C. E., 1967: Diffusion approximation to inertial energy transfer in isotropic turbulence. *Phys. Fluids*, **10**, 1409–1416, doi:10.1063/1.1762300.

Losch, M., D. Menemenlis, P. Heimbach, J.-M. Campin, and C. Hill, 2010: On the formulation of sea-ice models. Part 1: Effects of different solver implementations and parameterizations. *Ocean Modell.*, **33**, 129–144, doi:10.1016/j.ocemod.2009.12.008.

Luckman, A., T. Murray, R. de Lange, and E. Hanna, 2006: Rapid and synchronous ice-dynamic changes in east Greenland. *Geophys. Res. Lett.*, **33**, L03503, doi:10.1029/2005GL025428.

Magaldi, M. G., T. W. N. Haine, and R. S. Pickart, 2011: On the nature and variability of the East Greenland Spill Jet: A case study in summer 2003. *J. Phys. Oceanogr.*, **41**, 2307–2327, doi:10.1175/JPO-D-10-05004.1.

Marshall, J., A. Adcroft, C. Hill, L. Perelman, and C. Heisey, 1997: A finite-volume, incompressible Navier Stokes model for studies of the ocean on parallel computers. *J. Geophys. Res.*, **102**, 5753–5766, doi:10.1029/96JC02775.

Menemenlis, D., and Coauthors, 2005: NASA supercomputer improves prospects for ocean climate research. *Eos, Trans. Amer. Geophys. Union*, **86**, 89–96, doi:10.1029/2005EO090002.

Murray, T., and Coauthors, 2010: Ocean regulation hypothesis for glacier dynamics in southeast Greenland and implications for ice sheet mass changes. *J. Geophys. Res.*, **115**, F03026, doi:10.1029/2009JF001522.

Nguyen, A. T., D. Menemenlis, and R. Kwok, 2009: Improved modeling of the Arctic halocline with a subgrid-scale brine rejection parameterization. *J. Geophys. Res.*, **114**, C11014, doi:10.1029/2008JC005121.

Oltmanns, M., F. Straneo, G. W. K. Moore, and S. H. Mernild, 2014: Strong downslope wind events in Ammassalik, southeast Greenland. *J. Climate*, **27**, 977–993, doi:10.1175/JCLI-D-13-00067.1.

Price, J. F., and M. O. Baringer, 1994: Outflows and deep water production by marginal seas. *Prog. Oceanogr.*, **33**, 161–200, doi:10.1016/0079-6611(94)90027-2.

Rahmstorf, S., J. E. Box, G. Feulner, M. E. Mann, A. Robinson, S. Rutherford, and E. J. Schaffernicht, 2015: Exceptional twentieth-century slowdown in Atlantic Ocean overturning circulation. *Nat. Climate Change*, **5**, 475–480, doi:10.1038/nclimate2554.

Rietbroek, R., S.-E. Brunnabend, J. Kusche, J. Schröter, and C. Dahle, 2016: Revisiting the contemporary sea-level budget on global and regional scales. *Proc. Natl. Acad. Sci. USA*, **113**, 1504–1509, doi:10.1073/pnas.1519132113.

Rignot, E., M. Koppes, and I. Velicogna, 2010: Rapid submarine melting of the calving faces of west Greenland glaciers. *Nat. Geosci.*, **3**, 187–191, doi:10.1038/ngeo765.

Rudels, B., E. Fahrbach, J. Meincke, G. Budéus, and P. Eriksson, 2002: The East Greenland Current and its contribution to the Denmark Strait overflow. *ICES J. Mar. Sci.*, **59**, 1133–1154, doi:10.1006/jmsc.2002.1284.

Sakov, P., F. Counillon, L. Bertino, K. A. Lisæter, P. R. Oke, and A. Korablev, 2012: TOPAZ4: An ocean-sea ice data assimilation system for the North Atlantic and Arctic. *Ocean Sci.*, **8**, 633–656, doi:10.5194/os-8-633-2012.

Seale, A., P. Christoffersen, R. I. Mugford, and M. O'Leary, 2011: Ocean forcing of the Greenland Ice Sheet: Calving fronts and patterns of retreat identified by automatic satellite monitoring of eastern outlet glaciers. *J. Geophys. Res.*, **116**, F03013, doi:10.1029/2010JF001847.

Shepherd, A., and Coauthors, 2012: A reconciled estimate of ice sheet mass balance. *Science*, **338**, 1183–1189, doi:10.1126/science.1228102.

Straneo, F., and P. Heimbach, 2013: North Atlantic warming and the retreat of Greenland's outlet glaciers. *Nature*, **504**, 36–43, doi:10.1038/nature12854.

——, and C. Cenedese, 2015: The dynamics of Greenland's glacial fjords and their role in climate. *Annu. Rev. Mar. Sci.*, **7**, 89–112, doi:10.1146/annurev-marine-010213-135133.

——, and Coauthors, 2013: Challenges to understanding the dynamic response of Greenland's marine terminating glaciers to oceanic and atmospheric forcing. *Bull. Amer. Meteor. Soc.*, **94**, 1131–1144, doi:10.1175/BAMS-D-12-00100.1.

Sutherland, D. A., and R. S. Pickart, 2008: The East Greenland Coastal Current: Structure, variability, and forcing. *Prog. Oceanogr.*, **78**, 58–77, doi:10.1016/j.pocean.2007.09.006.

——, F. Straneo, G. B. Stenson, F. J. M. Davidson, M. O. Hammill, and A. Rosing-Asvid, 2013: Atlantic water variability on the SE Greenland continental shelf and its relationship to SST and bathymetry. *J. Geophys. Res. Oceans*, **118**, 847–855, doi:10.1029/2012JC008354.

——, ——, and R. S. Pickart, 2014: Characteristics and dynamics of two major Greenland glacial fjords. *J. Geophys. Res. Oceans*, **119**, 3767–3791, doi:10.1002/2013JC009786.

Thomas, R., E. Frederick, W. Krabill, S. Manizade, and C. Martin, 2009: Recent changes on Greenland outlet glaciers. *J. Glaciol.*, **55**, 147–162, doi:10.3189/002214309788608958.

van den Broeke, M., and Coauthors, 2009: Partitioning recent Greenland mass loss. *Science*, **326**, 984–986, doi:10.1126/science.1178176.

Velicogna, I., and J. Wahr, 2013: Time-variable gravity observations of ice sheet mass balance: Precision and limitations of the GRACE satellite data. *Geophys. Res. Lett.*, **40**, 3055–3063, doi:10.1002/grl.50527.

von Appen, W.-J., and Coauthors, 2014: The East Greenland Spill Jet as an important component of the Atlantic meridional overturning circulation. *Deep-Sea Res. I*, **92**, 75–84, doi:10.1016/j.dsr.2014.06.002.